



## Microstructure refinement of a cast high entropy alloy by thermomechanical treatments

Ricardo Henrique Buzolin<sup>a,b,\*</sup>, Markus Masswohl<sup>a,b</sup>, Franz Miller Branco Ferraz<sup>a,b</sup>, Konrad Chrzan<sup>c</sup>, Tomasz Dudziak<sup>c</sup>, Maria Cecilia Poletti<sup>a,b</sup>

<sup>a</sup> Christian Doppler Laboratory for Design of High-Performance Alloys By Thermomechanical Processing, Kopernikusgasse 24, 8010, Graz, Austria

<sup>b</sup> Institute of Materials Science, Joining and Forming at Graz University of Technology, Kopernikusgasse 24/I, 8010, Graz, Austria

<sup>c</sup> Sieć Badawcza Łukasiewicz - Krakowski Instytut Technologiczny, ul. Zakopiańska 73, 30-418, Kraków, Poland

### ARTICLE INFO

#### Keywords:

High entropy alloys  
Thermomechanical treatments  
Recrystallisation  
Microstructure refinement  
Hot deformation  
Annealing

### ABSTRACT

This work investigates the hot compressive behaviour of a cast high entropy alloy. The alloy is subjected to four different thermomechanical treatments to refine the as-cast microstructure: hot compression tests at constant strain rates ( $0.001\text{s}^{-1}$  and  $1\text{s}^{-1}$ ), hot compression tests with strain rate jumps (between  $0.001\text{s}^{-1}$  and  $1\text{s}^{-1}$ ), multi-stage hot deformation with holding intervals of 1 and 5 min, and hot compression at  $0.1\text{s}^{-1}$  followed by annealing. The three first tests were carried out at  $1100\text{ }^{\circ}\text{C}$  and the deformation step of the last type was carried out at  $1050\text{ }^{\circ}\text{C}$  followed by annealing at  $1150\text{ }^{\circ}\text{C}$ . The deformation at  $0.001\text{s}^{-1}$  promotes dynamic recrystallisation. Dynamic recrystallisation occurs when jumping from  $1\text{s}^{-1}$  to  $0.001\text{s}^{-1}$  and does not occur if the jump is from  $0.001\text{s}^{-1}$  to  $1\text{s}^{-1}$ . Multi-stage interrupted tests show that 1 min holding between the stages promote dynamic recrystallisation, while static recrystallisation occurs more pronouncedly for 5 min inter-stage holding. Due to the large initial grain size, deformation does not occur homogeneously within the grains, and heterogeneous static recrystallisation occurs within the deformed specimen. Whether the alloy is solution heat treated or deformed in the as-cast condition does not affect the recrystallisation behaviour. Overall, refining the coarse cast microstructure of the investigated alloy is possible, although more deformation steps are needed to produce a homogeneous microstructure.

### 1. Introduction

High entropy alloys (HEAs) are a new class of material that received considerable attention in recent years [1–4]. They are multi-principal elemental alloys, where the alloy is composed of four or more primary elements forming simple solid solution phases [5]. Promising properties for structural applications can be listed, such as high fracture-resistant for cryogenic applications [6], high compressive strength [7], and a high strength-ductility ratio [8]. The functional properties of high HEAs have also been investigated and showed promising results for catalytical materials [9,10], magnetic materials [11–13] and coatings for high-temperature or high oxidation resistance [14,15]. However, some limitations hinder the application of HEAs as a structural material. HEAs have only shown a few examples of notable breakthroughs in strength-to-ductility [16] or high-creep resistance [17]. However, the cryogenic and low-temperature mechanical properties seem more

promising [2].

Two main issues can affect the processability of HEAs. Firstly, HEAs are cast using arc melting furnaces with a protective atmosphere, typically requiring several re-melts to avoid macro-segregation in the ingots. The next challenge is to thermomechanically process these alloys. Several classes of HEAs are cold-formable via transformation induced by plasticity (TRIP) or twinning induced by plasticity (TWIP) mechanisms and have notable high strength-ductility synergy [2,18,19]. Those alloys are aimed for room or low-temperature applications because the cold deformed microstructure formed during processing is unstable at high temperatures. The HEAs that cannot be easily processed at room temperature or that are aimed at high-temperature applications require specific thermomechanical treatments.

There are several categories of HEAs. From the chemical composition and crystal structure, they can be mainly classified as single-phase or multi-phase alloys [16]. The single phase is typically face-centred cubic

\* Corresponding author. Christian Doppler Laboratory for Design of High-Performance Alloys By Thermomechanical Processing, Kopernikusgasse 24, 8010, Graz, Austria.

E-mail address: [ricardo.buzolin@tugraz.at](mailto:ricardo.buzolin@tugraz.at) (R.H. Buzolin).

<https://doi.org/10.1016/j.msea.2023.144931>

Received 18 January 2023; Received in revised form 13 March 2023; Accepted 17 March 2023

Available online 20 March 2023

0921-5093/© 2023 The Authors. Published by Elsevier B.V. This is an open access article under the CC BY license (<http://creativecommons.org/licenses/by/4.0/>).

(FCC) or body-centred cubic (BCC) [16]. The matrix of multi-phase HEAs can also be FCC or BCC, although some hexagonal closed-packed (HCP) phases have also been proposed [20,21]. Other phases with more complex structures can be formed in multi-phase HEAs [22]. In addition, they can be classified from the strengthening mechanisms point of view [2], such as TWIP, TRIP, spinodal transformation, dual-phase, and maraging, among other types [2]. Several works reported the thermomechanical behaviour of single-phase FCC HEAs [23–31]. In those alloys, discontinuous dynamic recrystallisation (DDRX) occurs [30,32–34] due to their typical low stacking fault energy [35–37]. However, inter-dependencies of the dynamic (when a load is applied) and static (without load) mechanisms on the microstructure formation during the thermomechanical processes were not yet investigated. Specifically, a clear strategy is missing to define the processing steps aiming at a possible implementation on a large scale.

This work aims to provide a guideline for refining the grains of as-cast HEAs by thermomechanical treatments. A single-phase FCC-based HEA is chosen for this investigation. Firstly, the substructures formed during deformation at high temperatures provides knowledge about the associated stored energy. Then, different paths of hot deformation and annealing are tested to elucidate how the microstructure is restored at high temperatures: single-step at constant strain rate, strain rate jumps, multi-stage deformation, and hot deformation followed by annealing. Finally, the role of thermomechanical history in microstructural evolution and grain refinement is discussed.

## 2. Experimental procedure

An 10Al, 17Co, 18Cr, 18Fe, 37Ni (at.%) high entropy alloy was cast using an induction-melting furnace. First, pure elemental metals were added to the melt, preheated around 1550 °C, under a protective atmosphere of Ar. Next, the melt was manually stirred and poured into a silicon oxide-based mold internally coated with aluminium oxide, preheated at 900 °C, and left cooled in air.

Cylindrical samples of the cast ingot were cut with 10 mm diameter and 15 mm length. Hot compression tests were carried out using a Gleeble® 3800-GTC thermomechanical simulator. K-type thermocouples welded at the surface of the samples measured and controlled the temperature. A heating rate of 5 °C/s and a soaking time before deformation of 3 min was used. A 300 µm thick graphite foil and 200 µm thick molybdenum sheet were placed between the sample and the anvils to minimise the temperature gradient and friction during the tests. All samples were water quenched after testing to preserve the microstructure for further analysis. Four types of tests were carried out:

- Hot compression at 1100 °C up to 0.85 of strain for strain rates of  $0.001\text{s}^{-1}$  and  $1\text{s}^{-1}$  for I) the as-cast condition and II) solution heat treated at 1150 °C for 24 h.
- Strain rate jump tests at 1100 °C to 0.85 strain from  $0.001\text{s}^{-1}$  to  $1\text{s}^{-1}$  and from  $1\text{s}^{-1}$  to  $0.001\text{s}^{-1}$  after reaching the strain of 0.425 for I) the as-cast condition and II) solution heat treated at 1150 °C for 24 h.
- Multi-stage hot compression tests at 1100 °C and  $1\text{s}^{-1}$ : the samples were deformed in strain intervals of 0.05 and held for 1 or 5 min between the deformation steps.
- Hot compression at 1000 °C and  $0.1\text{s}^{-1}$  up to 0.85 strain followed by annealing at 1150 °C for 30 min and 180 min in a furnace.

The as-cast samples and the ones deformed at elevated temperatures were cut and metallographically prepared by grinding from 320 up to 2000 grit and polishing using colloidal silica suspension (OP-S). Optical microscopy was carried out using a Zeiss Axio microscope. The samples were etched using a 100 ml distilled water, 25 ml 32% hydrochloric acid and 5 g of copper (II) sulphate solution to reveal the microstructure. As polished samples were examined using scanning electron microscopy (SEM) assisted by electron backscattered diffraction (EBSD) and energy-dispersive X-ray spectroscopy (EDX). The EBSD data was collected using

an EDAX Apex system using a Hikari Plus EBSD camera. The samples hot-deformed after 24 h solution heat treatment at 1150 °C were analysed using EDX, while selected as-cast hot-deformed samples were characterised using EDX and EBSD. EBSD maps of  $(2\text{ mm})^2$  and step size of 2 µm were measured for the hot deformed samples. The EBSD measurement was evaluated using OIM DataAnalysis 8.6. The confidence index of the grains was first standardised for a minimum grain size of 5 points. Then, points of confidence indexed below 0.2 were cleaned by correlation with the neighbours. A misorientation angle of 15° was considered the transition angle between low to high-angle grain boundaries. The kernel average misorientation (KAM) was obtained using the first nearest neighbour. The  $\Sigma 3$  boundaries were calculated using a tolerance of  $15 \cdot (\pi/\Sigma)^{0.5}$ . Finally, the dynamically recrystallised grains were partitioned from the deformed ones for the hot deformed samples. Grain orientation spread was calculated considering a grain surrounded by high angle grain boundaries

## 3. Results

The investigated material consists of a single-phase matrix formed by large grains, as shown in Fig. 1 a,b for the upper and bottom region of the ingot, respectively. Aluminium oxide inclusions are also embedded in the matrix, as indicated by the arrows in Fig. 1. They are formed due to the oxidation of the Aluminium added to the melt during casting, as also reported for similar alloys [38,39]. Micro-pores are also present in small amounts and scattered regions of the samples. Microsegregation is also present. Aluminium and nickel enrich the interdendritic spacing, while iron, chromium and cobalt enrich the inner part of the dendritic cells.

The flow curves and microstructure of the HEA deformed at high temperatures are described in the following sections. Finally, the effect of the thermomechanical treatment history on grain refinement is presented.

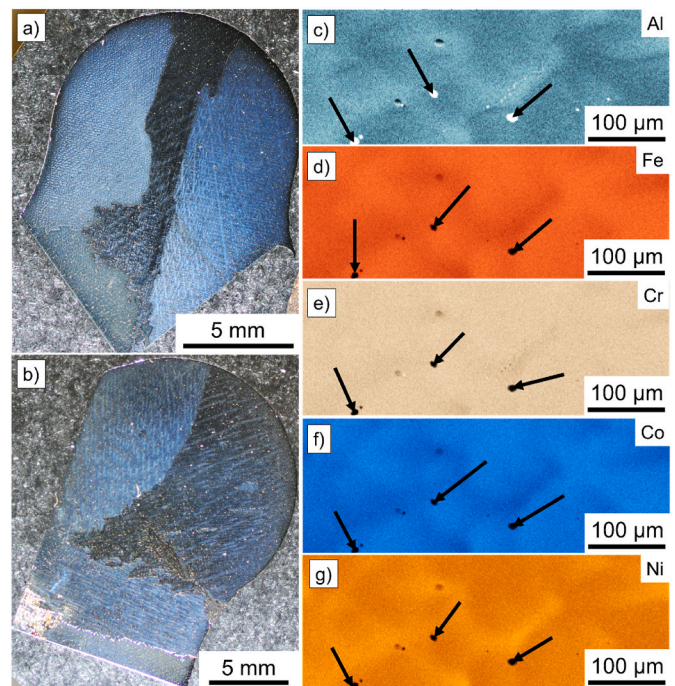


Fig. 1. Optical micrographs of the: a) upper part of the ingot; b) bottom part of the ingot. Energy dispersive X-ray spectroscopy (EDX) maps of the as-cast high entropy alloy: c) Aluminium; d) Iron; e) Chromium; f) Cobalt; g) Nickel. Black arrows indicate aluminium oxide inclusions.

### 3.1. Hot compression at constant strain rates and strain rate jump

Fig. 2 shows the flow curves for the hot compressed HEA. A significant variation of the flow curves for the different samples, related to the large grain size of the cast material, is shown in Fig. 2b. The flow curves of the tests carried out for a constant strain rate, and strain rate jumps are shown in Fig. 2a. There are no notable differences between the samples tested in the as-cast conditions (solid lines) and the ones tested after solution heat treatment (SHT, dashed lines). The alloy rapidly accommodates the stresses due to the change in strain rate during the strain rate jump tests. The initial work hardening is small for the investigated conditions.

Fig. 3 shows the micrographs of the cross-sections of the as-cast deformed samples. The as-cast grains elongate after hot compression. The areas marked by the red lines indicate the regions where dynamic recrystallisation took place. Dynamic recrystallisation is not observed for the cross-section of the sample deformed at 1100 °C and 1s<sup>-1</sup> (Fig. 3c) nor for the strain rate jump from 0.001s<sup>-1</sup> to 1s<sup>-1</sup> (Fig. 3d). The recrystallisation grade seems slightly higher for the strain rate jump from 1s<sup>-1</sup> to 0.001s<sup>-1</sup> (Fig. 3b) compared to the deformation at the constant strain rate of 0.001s<sup>-1</sup> (Fig. 3a). The recrystallised grains are formed along the initial grain boundaries, which occurs mainly in the regions near the centre of the sample. The temperature is lower at the edges touching the anvils than at the centre of the sample. Together with the friction between the sample and the anvil, both aspects promote larger deformation at the centre of the sample than in the region near the anvils.

Fig. 4 shows the EBSD maps for the centre areas of the cross-section of the as-cast samples deformed at 1100 °C and 0.001s<sup>-1</sup> (Fig. 4a-d) and for the strain rate jump from 1s<sup>-1</sup> to 0.001s<sup>-1</sup> (Fig. 4e-h). The inverse pole figure maps in Fig. 4a,e show that the dynamically recrystallised grains slightly elongate perpendicular to the loading direction. Fig. 4b,f shows the kernel average misorientation (KAM) maps. The high KAM values (green regions) within the dynamically recrystallised grains are related to their further deformation. Conversely, the dynamically recrystallised grains with low KAM (blue regions in Fig. 4b,f) and GOS (grains in blue with GOS smaller than 0.5 in Fig. 4c,g) values are freshly recrystallised grains formed at higher strains. The boundary maps in Fig. 4d,h show the grain structure and substructures. The red lines in Fig. 4d,h indicate the low-angle grain boundaries (LAGB). LAGBs are organised in a polygonal-like substructure. The green lines indicate the CSL  $\Sigma 3$  boundaries (recrystallisation twins) in Fig. 4d,h, formed by DDRX.

### 3.2. Multi-stage interrupted hot compression

Fig. 5 shows the stress as a function of time and strain for two as-cast samples after multi-stage compression at 1s<sup>-1</sup> with 1 min and 5 min of

holding stage period. The stresses achieved during the steps of hot compression are rapidly relieved during intermediate holding treatments, Fig. 5a,c.

The evolution of the stress during the intermediate holding stage is evaluated and shown in Fig. 6. Assuming that the total strain during an isothermal test is the sum of the elastic and plastic components, Equation (1) and Hook's law can be applied. Then, the plastic strain can be calculated according to Equation (2). Furthermore, the derivative of Hook's law can express the plastic strain rate as a function of the stress rate, Equation (3).

$$\varepsilon = \varepsilon_p + \varepsilon_e \quad \text{Equation 1}$$

$$\varepsilon_p = -\frac{\sigma}{E} \quad \text{Equation 2}$$

$$\dot{\varepsilon}_p = -\frac{\dot{\sigma}}{E} \quad \text{Equation 3}$$

A Young modulus of 160 GPa at the tested temperature was adopted from a similar HEA [40]. The calculated plastic strain rate evolutions are shown in Fig. 6(a and d) for the inter-stage holding of 1 and 5 min, respectively. The strain rates higher than 10<sup>-4</sup>s<sup>-1</sup> show that stress relaxation occurs fast at high temperatures. The plastic strain rates are higher in the first holding stages, and the relaxation rate decreases with the strain increment, as shown in Fig. 6b,d. The differences among stages are minor, although there is a slight difference in the steady-state stresses. The steady-state condition was not reached even up to 5 min for the last holding steps, Fig. 6d. The relaxation occurs faster for the test with an inter-stage holding of 1 min compared to the tests where the holding time was 5 min (Fig. 6b,d).

Fig. 7 shows the cross-sections of the as-cast samples tested in multi-stage compression samples at 1s<sup>-1</sup>. Like the microstructure of the deformed samples shown in Fig. 3, the prior grains got elongated, while the recrystallised grains are primarily located along the initial grain boundaries. A smaller recrystallised region is observed for the 5 min multi-stage sample, Fig. 7b, compared to the 1 min multi-stage sample, Fig. 7a.

Fig. 9 shows the EBSD maps for an area in the cross-section's central region. The recrystallised grains shown in Fig. 9a-d for the multi-stage deformation with 1 min of inter-stage holding have lower KAM values than those shown in Fig. 4, as shown in the KAM distributions in Fig. 8.

Moreover, the deformed regions in both cases, 1 and 5 min inter-stage holding, have a less complex substructure than the substructure produced at constant strain rates and strain rate jump shown in Fig. 4. The black arrows and the dashed ellipse in Fig. 9a,e indicate newly formed grains near or surrounding the oxide inclusion and recrystallised grains formed along the prior grain boundary, respectively. The grains formed near the oxide inclusions are related to the mechanism of particle-stimulating nucleation. Both samples in Fig. 7 showed a level of

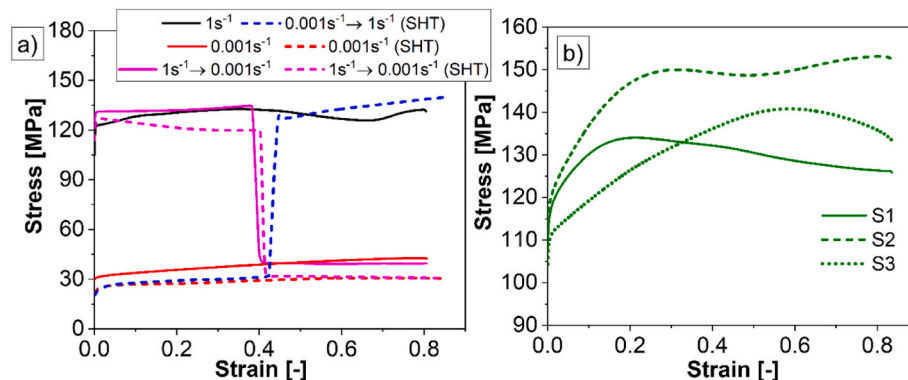


Fig. 2. Flow curves for the hot compression tests performed at a) 1100 °C and at the constant strain rate of 0.001s<sup>-1</sup> and 1s<sup>-1</sup> as well as for strain rate jump tests; b) three repetitions at 1000 °C and 0.1s<sup>-1</sup>.

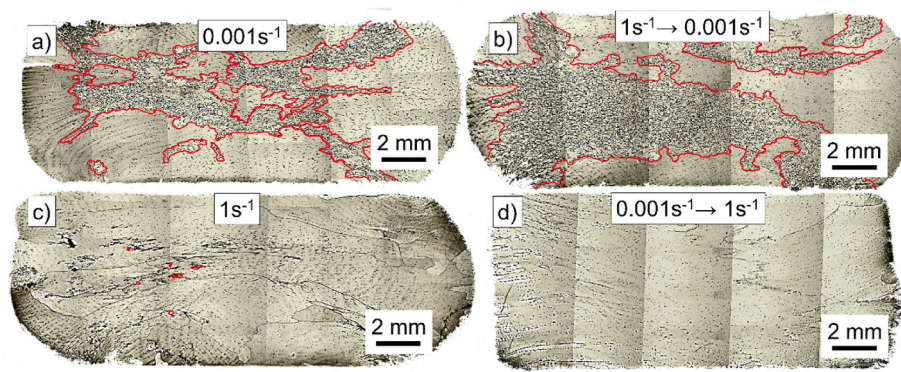


Fig. 3. Optical micrographs of the cross sections of the deformed samples at 1100 °C and a) 0.001 s<sup>-1</sup>; b) 1 s<sup>-1</sup> to 0.001 s<sup>-1</sup>; c) 1 s<sup>-1</sup>; d) 0.001 s<sup>-1</sup> to 1 s<sup>-1</sup>.

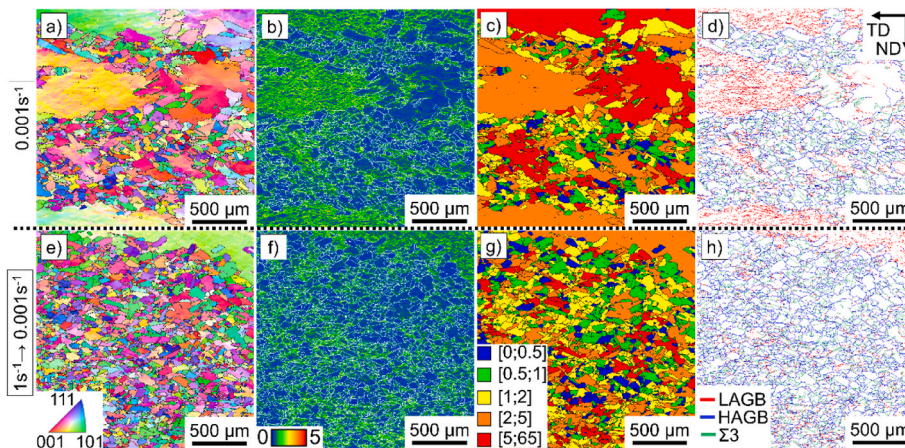


Fig. 4. Maps resulted from EBSD measurements of the samples deformed at 1100 °C and: a-d) 0.001 s<sup>-1</sup>; e-h) jump from 1 s<sup>-1</sup> to 0.001 s<sup>-1</sup>; showing the: a,e) inverse pole figure maps; b,f) KAM maps; c,g) GOS maps; d,h) boundary maps. The black and white lines in the inverse pole figure, GOS and KAM maps indicate all the HAGBs.

recrystallisation compared to the samples deformed at 1100 °C and 1 s<sup>-1</sup> in Fig. 4. The GOS maps in Fig. 9c show recrystallised grains with different misorientations (different colours) coming from all different stages of formation for the 1 min inter-stage. In contrast, Fig. 9g shows mostly GOS values below 1° for recrystallised grains after 5 min.

### 3.3. Static recrystallisation

As-cast samples deformed at 1000 °C and 0.1 s<sup>-1</sup> were further annealed at 1150 °C for 30 min and 180 min, and the cross-section micrographs are shown in Fig. 10. Fig. 10a shows the microstructure of the deformed HEA at 1000 °C and 0.1 s<sup>-1</sup>. The large and elongated grains are visible, and no dynamically recrystallised grains are present. The material partially recrystallises after 30 min at 1150 °C, Fig. 10b. Complete recrystallisation is nearly achieved after 180 min heat treatment at 1150 °C, Fig. 10c. However, the grain size is not homogeneous within the sample and is directly related to the distribution of stored energy within the specimen right after deformation. Regions where more dislocations were produced (larger strain in the middle of the sample due to barrelling) have higher stored energy and recrystallise first.

High stored energy promotes a high nucleation rate and high growth rate. If nucleation is high, the stored energy is rapidly consumed, and a fine microstructure is formed. If growth prevails, a coarse microstructure is produced. The red rectangle indicates the region where nucleation occurred first in Fig. 10b. Significant grain coarsening does not seem to occur after 180 min heat treatment in the areas where small

grains are present. The regions with large grains are mainly at the edge and in the dead zone, in both cases, regions with lower local strains. Thus, it can be concluded that, for this testing condition, nucleation instead of grain growth primarily controls static recrystallisation. Once it occurs, the grains rapidly grow, consuming all the deformed grains.

The EBSD maps in Fig. 11 show the microstructure in the central region in the samples shown in Fig. 10. The localised deformation around the inclusions is visible in Fig. 11c. The KAM maps in Fig. 11i show that the static recrystallisation entirely consumed the stored energy after 180 min and that some areas have not been fully recrystallised after 30 min. Fig. 11b,e,h shows the grain orientation spread (GOS) maps. Recrystallised grains are marked in blue with GOS values below 0.5°. Fig. 11f has slightly higher KAM values than the ones shown in Fig. 11i, also shown in the KAM distributions in Fig. 11j. The KAM maps indicate that all grains are recrystallised in Fig. 11i. Fig. 11h shows some grains with GOS values higher than 1°. The presence of LAGBs between two recrystallised grains leads to this difference. LAGBs typically have low mobility compared to HAGBs. Thus, the GOS and KAM maps can be used as indicator grains or regions that will be subjected only to coarsening (low KAM and GOS values) and regions or grains where: a) recrystallisation will still occur (grains with high KAM values) or b) grains that will likely consume the neighbour (the ones divided by LAGB despite low KAM values).

## 4. Discussion

The as-cast microstructure of the investigated HEA consists of large

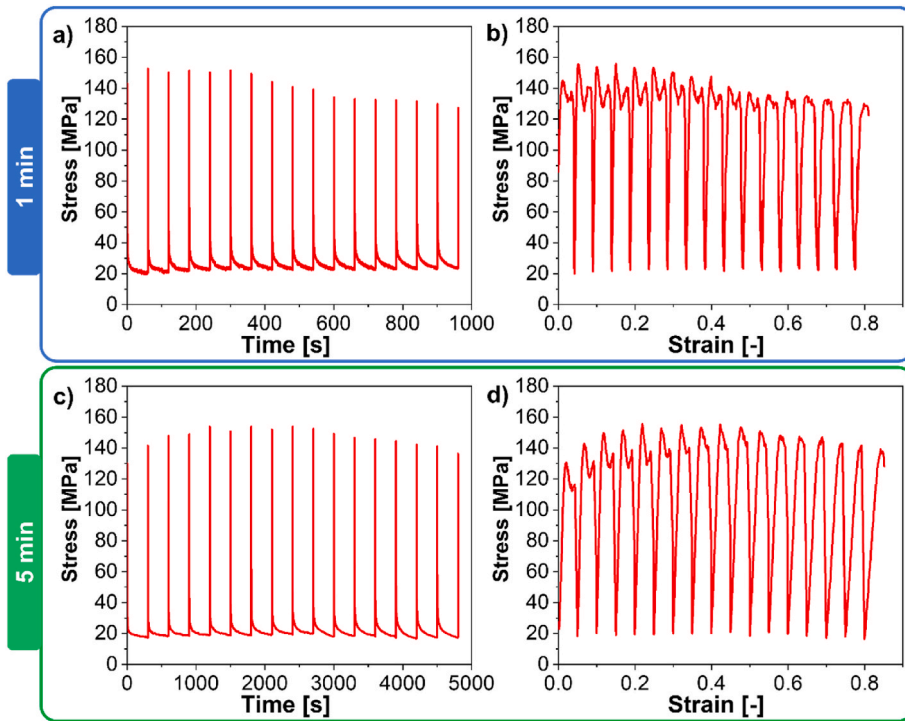


Fig. 5. Flow stress developed after compression at  $1s^{-1}$  with intermediate holding stage period of 1 min and 5 min, as a function of the time a,c) and the strain b,d).

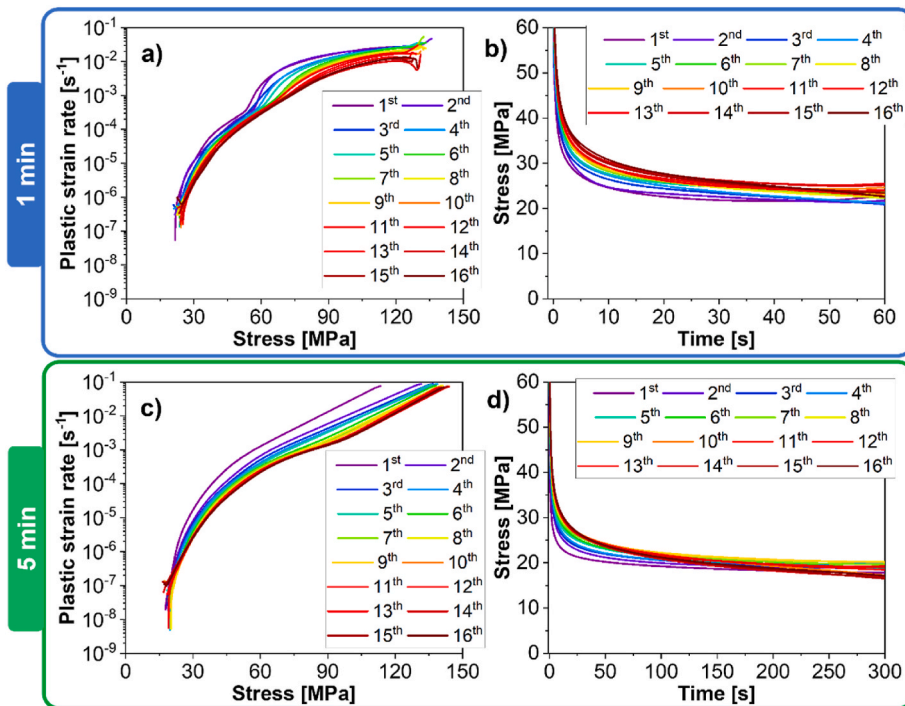


Fig. 6. Stress relaxation results: a,c) plastic strain rate over stress after the inter-stage periods of 1 and 5 min, respectively; b,d) stress evolution over time after the inter-stage periods of 1 and 5 min, respectively.

grains. This work focuses on the mechanisms of grain refinement at high temperatures, where steps of deformation and/or heat treatments are combined. As the first step, it is necessary to correlate the deformation mechanisms with the substructure formation and its associated stored energy at high-temperatures. Secondly, the mechanisms of static and dynamic recrystallisation are explained based on the consumption of the stored energy formed during deformation. Here, the role of

thermomechanical history is further discussed by comparing the results of the different thermomechanical treatments. Finally, the possible strategies for grain refinement and microstructure control via thermo-mechanical treatments are proposed for the investigated HEA.

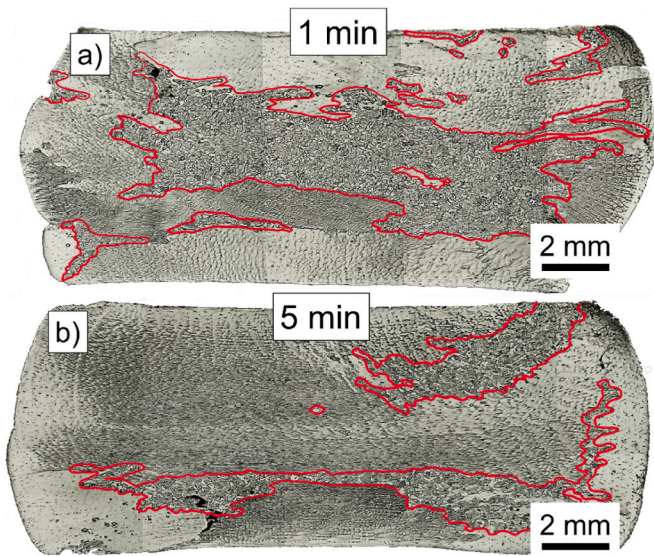


Fig. 7. Optical micrographs of the cross sections of the deformed samples at 1100 °C and  $1\text{s}^{-1}$  with inter-stage periods of a) 1 min; b) 5 min. The recrystallised region is marked in red. (For interpretation of the references to colour in this figure legend, the reader is referred to the Web version of this article.)

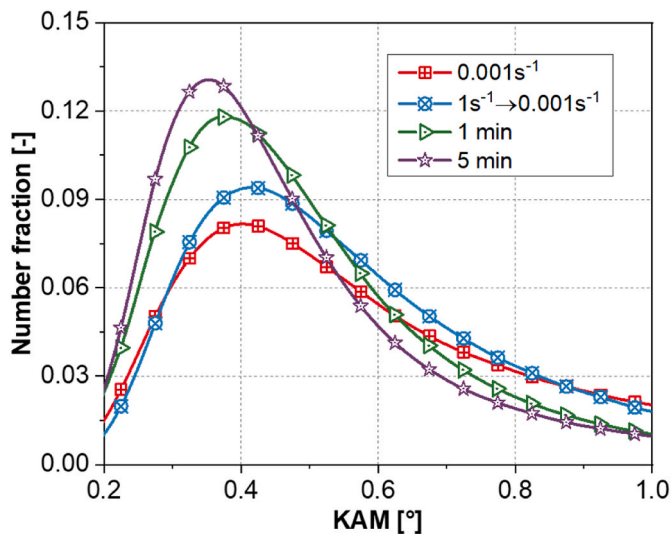


Fig. 8. Kernel average misorientation (KAM) distributions for the material deformed at 1100 °C and: I) at  $0.001\text{s}^{-1}$ , II) with strain rate jump from  $1\text{s}^{-1}$  to  $0.001\text{s}^{-1}$  and for the multi-stage deformation with intervals of holding of III) 1 and IV) 5 min.

#### 4.1. High-temperature deformed substructures

Work-hardening occurs because of the progressive dislocation density increment during plastic deformation. Dislocations multiply but also annihilate or are arranged in specific configurations. In the investigated alloys, dislocations accumulate in the vicinity of the oxides. In all cases, the plastic deformation accommodates by the movement of dislocations. The FCC HEAs based on 3D transitional elements are usually low-stacking fault energy materials [35–37]. Thus, the phenomena found in Nickel-based alloys [41] are expected to occur similarly in the investigated alloy. Fig. 12 shows the KAM maps for the deformed regions in different conditions.

A polygonal-like substructure is formed at the deformed grain shown in Fig. 12c. The multi-stage deformation presents a larger substructure with lower KAM values because of the static recovery during the inter-

stage holdings. Fig. 12a exhibit three regions with different general patterns for the substructure observed in the investigated alloy: I) accumulation of misorientation related to dislocation pile-ups around the oxide inclusions; II) bands of misorientation related to the dislocation glide in the slip systems for the local shear stresses and their pile-up; III) formation of a more established polygonal substructure due to dynamic recovery, which is also observed in Fig. 12b due to dynamic/static recovery.

#### 4.2. Mechanisms of recrystallisation

The investigated HEA dynamically recrystallises via DDRX forming  $\Sigma 3$  boundaries. The recrystallisation process consists of nucleation and growth of new grains during the plastic deformation at high temperatures. Typically necklace microstructure is formed if the starting microstructure is composed of large grains [41]. Since it is a dynamic process, the discontinuous dynamic recrystallised grains further deform, and many cycles of recrystallisation and subsequent deformation can occur until the load is released. After deformation, two phenomena can occur during heat treatments:

- Meta-dynamic recrystallisation: if dynamic recrystallisation occurs, new grains are formed. They are further deformed and accumulate stored energy. If this stored energy is not consumed dynamically, it will produce new grains during heat treatments [42]. The stored energy is consumed by nucleation and growth of the new grains. Meta-dynamic recrystallisation typically occurs faster than static recrystallisation [43].
- Static recrystallisation: when the initial un-deformed grains are subjected to plastic deformation, but no dynamic recrystallisation occurs, static recrystallisation of the deformed microstructure will occur, consuming it.

Several phenomena can play a role in the recrystallisation process, as summarised:

- Diffusion: although sluggish diffusion was reported for HEAs [44], it is mainly associated with Mn presence [45]. There is no Mn in the current alloy. Thus, all associated phenomena with diffusion, such as dislocation climb and grain boundary movement, are expected to be similar to the conventional alloy systems [45].
- Stored energy: it is the driving force for nucleation and growth and the controlling factor for dynamic and static recrystallisation in the investigated HEA. High stored energy caused by high dislocation density promotes fast grain growth. Once a grain nucleates, it rapidly grows, consuming the nearby deformed region, and the boundary movement decreases rapidly. If only a few grains nucleate because the stored energy is small, the grain boundary velocity is too small to consume the deformed material. The grain curvature is the driving force for grain coarsening, which is small for the formed grain size by recrystallisation. Thus, larger strains and/or higher temperatures would be required to promote an effective and homogeneous grain refinement for the investigated as-cast HEA.
- Grain size: the investigated HEA restores its microstructure by DDRX during hot deformation. Nucleation typically occurs at microstructural features such as grain boundaries or shear and deformation bands [41]. A large initial grain size results in low volumetric boundary density, reducing the overall nucleation rate. Moreover, deformation can occur heterogeneously within large grains, and some areas have higher stored energy than others. Since the investigated as-cast HEA has notably large grain sizes, dynamic recrystallisation requires large strains to start and be finished.

Consequently, the role of the process parameters on the recrystallisation behaviour are:

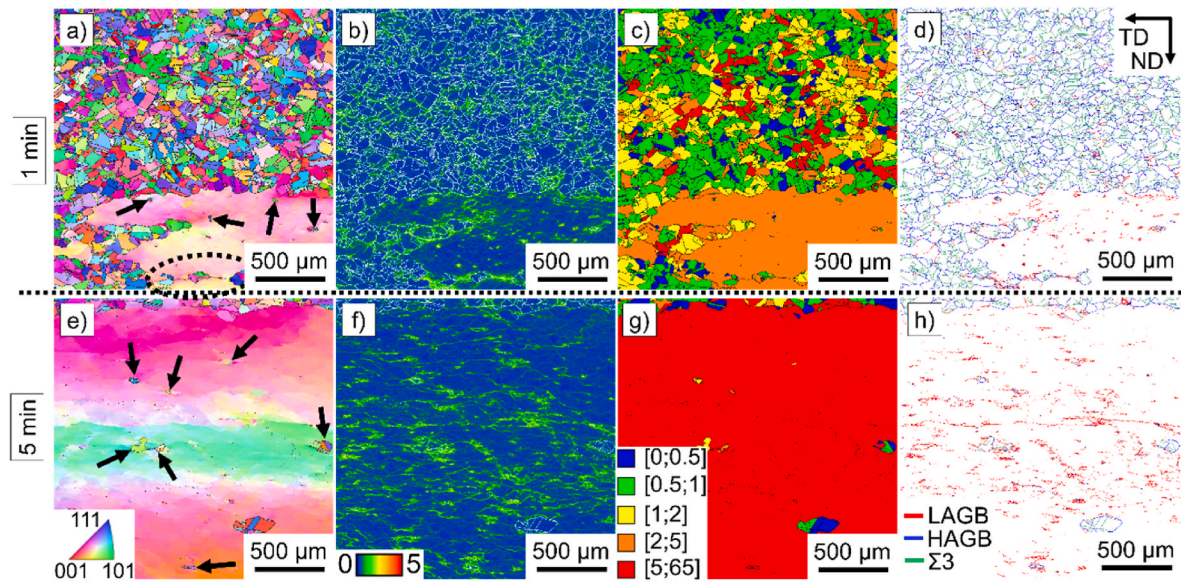


**Fig. 9.** Results of the EBSD measurements of the samples deformed at 1100 °C and  $1s^{-1}$  with inter-stage period: a-d) 1 min; e-h) 5 min, showing the: a,e) inverse pole figure (IPF) maps; b,f) KAM maps; c,g) GOS maps; d,h) boundary maps. The black and white lines in the IPF and KAM maps indicate all the HAGBs. The black arrows and the dashed ellipse in a,e) indicate grains formed in the vicinity of the oxides and recrystallised grains formed along a prior grain boundary, respectively.

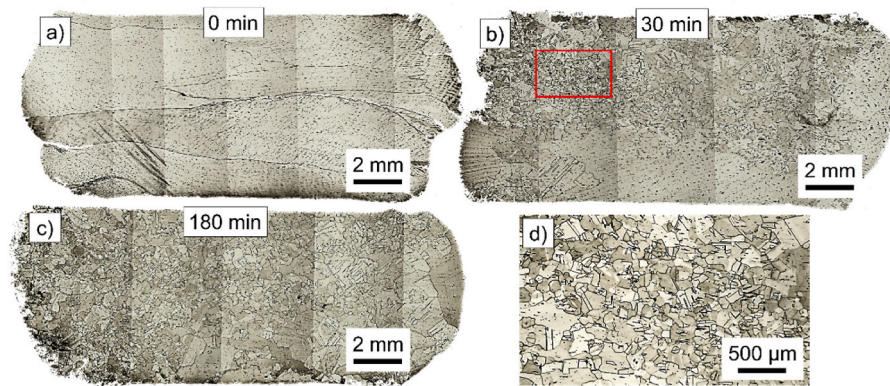


**Fig. 10.** Light micrographs of the cross-section of samples deformed at 1000 °C and  $0.1s^{-1}$  and annealed at 1150 °C for a) 0 min (as deformed); b) 30 min; c) 180 min.

- **Temperature:** regarding the steps of deformation, higher temperatures enhance DDRX due to the faster movement of grain boundaries and faster nucleation, although dynamic recovery is more pronounced. Regarding the steps of holding, higher temperatures also promote meta-dynamic recrystallisation or static recrystallisation for the same reason.
- **Strain rate:** faster deformation leads to higher dislocation density at the deformation steps. However, the time for DDRX is reduced considering a given total deformation, limiting nucleation and grain growth, thus DDRX. Faster deformation can, thus, lead to higher stored energy, which can be used in the subsequent steps of annealing to restore the energy either via meta-DDRX or static recrystallisation.
- **Total deformation:** the higher the total deformation, the more stored energy is produced, and the longer the time to promote DDRX. If DDRX is limited, higher total deformations facilitate static recrystallisation.
- **Inter-stage holding time:** the annealing time between steps of deformation defines the degree of statically or meta-dynamically recrystallised material. Longer times lead to more static or meta-dynamically recrystallisation. However, it also limits the stored

energy for the subsequent steps of deformation and consequently to DDRX.

#### 4.3. Effect of the thermomechanical history on the microstructure

Dynamic recovery is slow for low-stacking fault energy materials, such as the investigated alloy. Thus, it requires time to accommodate the change in the thermomechanical state. Figs. 2–4 show the comparison between the results of the tests at constant strain rate and for strain rate jump. There is a minor difference for the  $0.001s^{-1}$ , considering a given final strain rate ( $0.001s^{-1}$  or  $1s^{-1}$ ), indicating that the effect of the deformation history is not pronounced in the investigated alloy for the tested conditions.

On the other hand, the multi-stage tests affect the final microstructure. While the constant strain rate and strain rate jump results suggest that dynamic recrystallisation does not occur at  $1s^{-1}$ , recrystallised grains are found in the multi-stage tested samples after reaching the same total strain. The recrystallised grains can be formed: a) during deformation (dynamic recrystallisation) and/or b) during isothermal holding (meta-dynamic and/or static recrystallisation). Since it is not possible to distinguish between these two types, the experimental

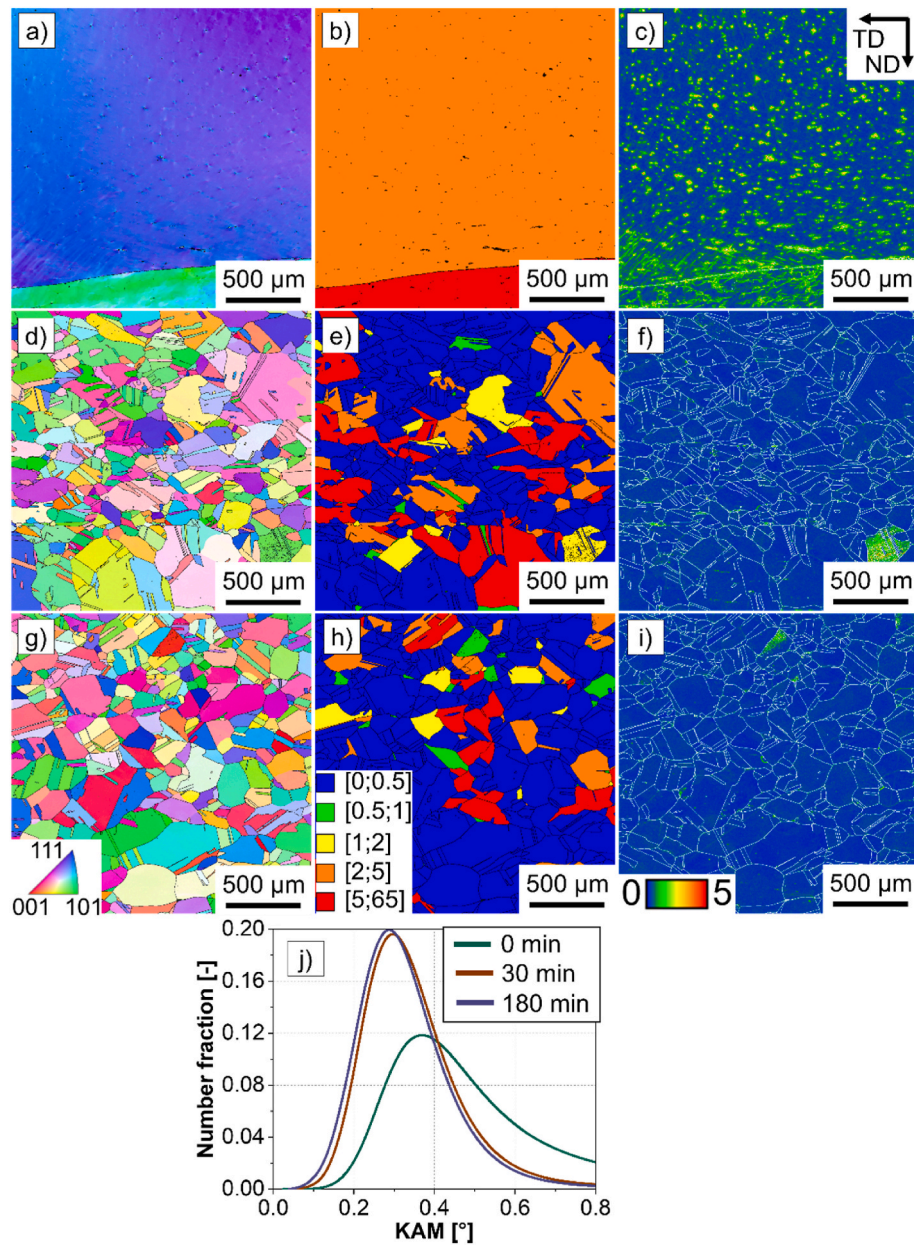


Fig. 11. Electron backscattered diffraction (EBSD) results for the as-cast samples deformed at 1000 °C and  $0.1s^{-1}$  and annealed at 1150 °C for a-c) 0 min (as-deformed); d-f) 30 min; g-i) 180 min, showing the: a,d,g) IPF maps; b,e,h) GOS maps; c,f,i) KAM maps; j) KAM distributions. The black lines in the inverse pole figure and GOS maps and the white lines in the KAM indicate all the HAGBs.

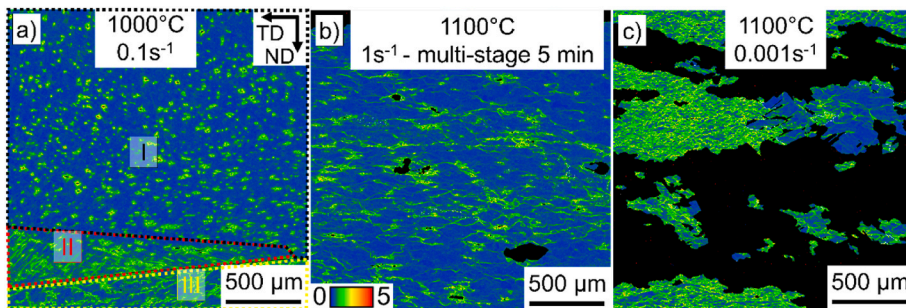


Fig. 12. Electron backscattered diffraction (EBSD) results showing the kernel average misorientation (KAM) maps for the HEA deformed at a) 1000 °C and  $0.1s^{-1}$ ; b) 1100 °C and  $1s^{-1}$  for the 5 min multi-stage treatment; c) 1100 °C and  $0.001s^{-1}$ . The red dashed marked region I) in b) correspond to the accumulation of KAM around the oxide inclusions. Regions II) and III) in b) correspond to regions with a band-like and polygonal-like substructure, respectively. (For interpretation of the references to colour in this figure legend, the reader is referred to the Web version of this article.)

comparison between the tests carried out using 1 min and 5 min holding stages can be used to elucidate the restoration mechanisms. During holding, both, the static recovery and static recrystallisation reduce the dislocation density, although the recrystallised regions have orders of magnitude lower dislocation density than recovered ones. Recrystallised grains are present in both 1 and 5 min inter-stage holding times, contrasting with the absence of recrystallised grains for the deformed HEA at the constant strain rate of  $1\text{s}^{-1}$  (Fig. 3c). The proposed mechanism is shown in Fig. 13:

- During 1 and 5 min of holding, static recrystallisation and static recovery occur. The dislocation density decreases, and the amount of high-angle grain boundaries increases. The longer the time, the smaller the dislocation density and the larger the amount of new HAGBs
- Further deformation produces DDRX at the HAGBs, if the stored energy is large enough.
- The critical strain for DDRX is decreased by the appearance of new grains formed at the inter-stages. The critical strain for DDRX of the sample deformed in a single deformation step is not reached because of the large grains and the large strain hardening needed.

#### 4.4. Chemical homogeneity

Fig. 1 shows microsegregation in the as-cast condition before deformation. Comparatively, Fig. 14 shows EDX compositional maps of the deformed samples. Three cases with large exposure to high temperatures are chosen: hot deformation of the as-cast condition at a constant strain rate at  $1100\text{ }^{\circ}\text{C}$  and  $0.001\text{s}^{-1}$  (case I), multi-stage hot deformation of the as-cast condition at  $1100\text{ }^{\circ}\text{C}$  and  $1\text{s}^{-1}$  with inter-deformation steps of 5 min (case II), and a sample solution heat treated at  $1150\text{ }^{\circ}\text{C}$  for 24 h followed by hot deformation at  $1100\text{ }^{\circ}\text{C}$  and  $0.001\text{ s}^{-1}$  (case III). No notable differences are observed between cases I and II. There is no clear evidence that one or more elements get better distributed after deformation. The segregation zones seen in the material before deformation in the as-cast condition (Fig. 1) get elongated perpendicular to the deformation direction (ND) in cases I and II. The micro-segregation reduces after solution heat treatment but is not entirely eliminated and is also seen in case III.

The distribution of the elements and the boundaries are shown for the as-cast sample deformed at  $0.001\text{s}^{-1}$  in Fig. 15. There is no clear relationship between the chemical segregation and the formed  $\Sigma 3$  boundaries (blue boundaries in Fig. 15). However, there seems to be a relationship between the presence of the other HAGBs (black boundaries in Fig. 15) and the segregation lines, as shown in the regions enriched in

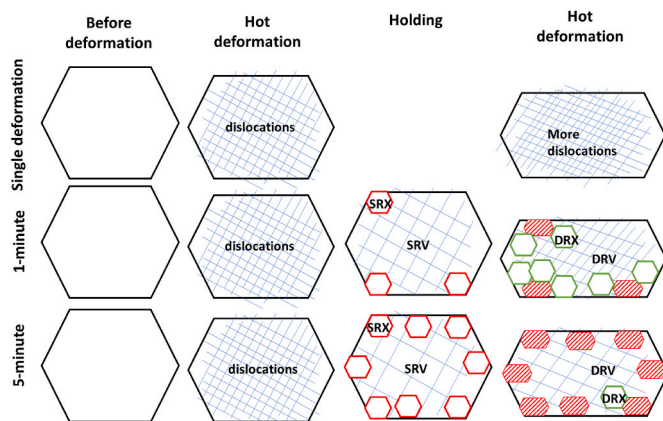


Fig. 13. Schematic representation of the interdependency between static recovery (SRV), static recrystallisation (SRX), and discontinuous dynamic recrystallisation (DDRX) for the multi-stage treatments compared to the single deformation.

Al and Ni and lean in Fe and Co. The differences in local chemical composition may also play a role in the movement of HAGBs during recrystallisation.

#### 4.5. Thermomechanical treatments strategies for grain refinement

Regarding a thermomechanical treatment that has the best grain refinement effect, a compromise between deformation and holding is needed. The effect of the processing parameters on grain refinement can be summarised as:

- Temperature: higher temperatures increase the nucleation and grain growth rate of discontinuous dynamic, post-dynamic and static recrystallisation considering a given stored energy. Therefore, an optimum grain refinement strategy must combine maximising nucleation rate and avoiding extensive grain growth.
- Strain rate: high strain rates typically retard dynamic grain refinement for a give temperature and strain but high strain rates yield high stored energy, which can be used to promote high nucleation rate in a controlled grain growth condition during annealing.
- Total deformation: it is typically beneficial for grain refinement since DDRX is a function of the deformation, as well as it gives the remaining stored energy for recrystallisation during steps of annealing.
- Inter-stage holding time: the combination of strain rate, strain and temperature gives the stored energy for grain refinement in annealing. The inter-stage holding promotes nucleation of new grains by a combination of static and dynamic recrystallisation, which can be beneficial for grain refinement.

All samples hot compressed in this work were deformed up to an approximate true strain of 0.85. It is relatively small for typical industrial forming processes, but it provides a guideline of how a thermo-mechanical treatment can be designed to refine the as-cast microstructure:

- The hot deformation at constant strain rates shows that grain refinement is only achieved at low strain rates since the onset of DDRX occurs at higher deformation times. Deforming first at high deformation speeds followed by a jump to low strain rates can enhance DDRX in the second step.
- Inter-stage steps can promote static and dynamic recrystallisation. However, only short holding times seem favourable for dynamic recrystallisation. For industrial applications, it may be challenging. In this work, an inter-stage strain of 0.05 was used. Larger inter-stage strains can likely lead to better refinement of grains.
- Static restoration: large heat treatment times seem required to recrystallise the material effectively at the tested temperatures after deformation at  $1000\text{ }^{\circ}\text{C}$ .

Thus, two main strategies for efficiently refine the cast grain structure can be followed:

- Strategy I: since a maximum nucleation rate and minimum grain growth is the desired strategy to achieve grain refinement, many initial passes at low temperatures, where the stored energy is accumulated, followed by finals passes at higher temperatures in a controlled exposed time can be a suitable strategy.
- Strategy II: one initial step of deformation at low strain rates can be used to form new grains by dynamic recrystallisation. From this point, one or two more steps where higher strain rates are achieved, and the material is annealed to meta-dynamically and/or statically recrystallise the microstructure.

Since grain coarsening is limited due to Al and Ni segregation, the grain size can be controlled by:

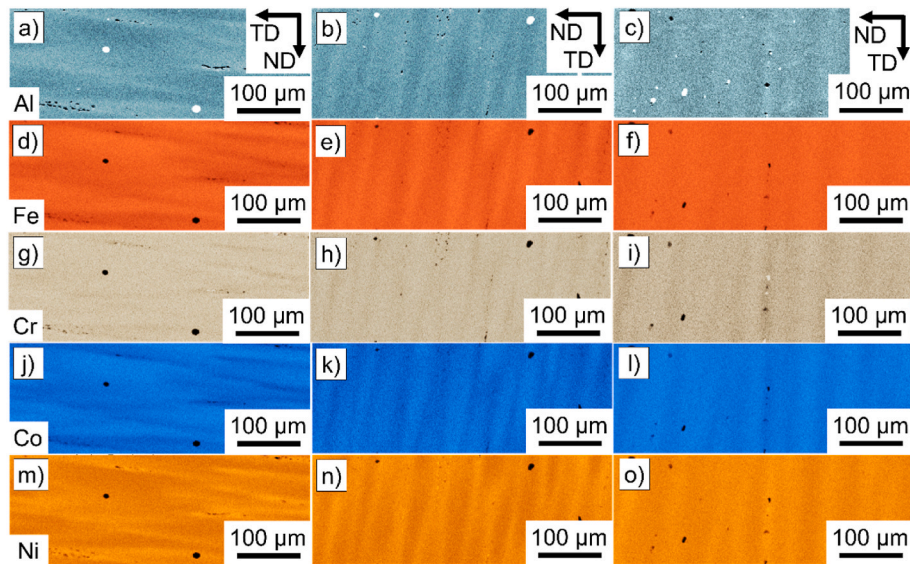


**Fig. 14.** EDX maps of a-c) Al; d-f) Fe; g-i) Cr; j-l) Co; m-o) Ni; for the deformed alloy at a,d,g,j,m) the constant strain rate of  $0.001s^{-1}$  for the as-cast condition; b,e,h,k,n) multi-stage deformation at  $1s^{-1}$  for 5 min holding for the as-cast condition; c,f,i,l,o) the constant strain rate of  $0.001s^{-1}$  for the solution heat-treated condition.

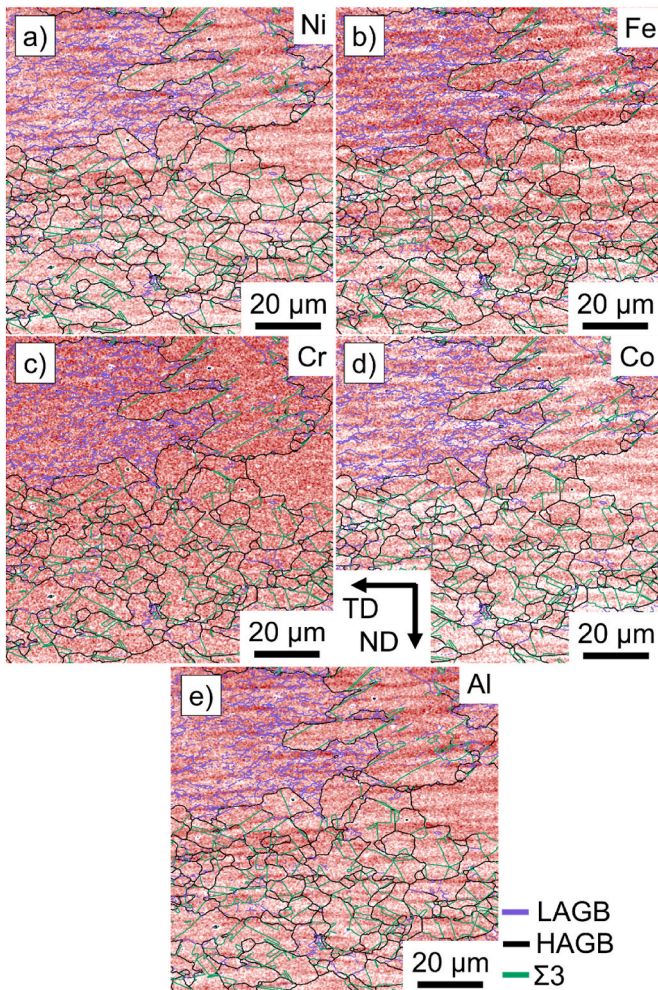


**Fig. 15.** Energy dispersive X-ray spectroscopy (EDX) maps for the as-cast alloy deformed at a constant strain rate of  $0.001s^{-1}$  of a) Nickel; b) Iron; c) Chromium; d) Cobalt; e) Aluminium.

- Enhancing the nucleation rate by producing a deformed microstructure with high stored energy and holding for short times at high temperatures.
- Controlling grain growth and coarsening: if the meta-dynamic or static recrystallisation is stopped at the early stage, where many nuclei are produced, a second step at low temperatures can be used to achieve complete recrystallisation.

## 5. Conclusions

The complex interactions involved in thermomechanical treatments of HEAs are investigated for an FCC single-phase alloy. The deformation mechanisms at elevated temperatures are compared and related to the substructure formations. The microstructure is restored at high temperatures via discontinuous dynamic recrystallisation during deformation, while meta-dynamic or static recrystallisation occurs during inter-stage steps and/or annealing. The obtained results allow drawing the following conclusions:

- The nucleation rate strongly controls the discontinuous dynamic recrystallisation for the investigated alloy and it mainly occurs along the grain boundaries and in the vicinity of oxide inclusions. A strain rate jump from high to low strain rates can accelerate discontinuous dynamic recrystallisation in the second step as the dislocations are not rapidly dynamically recovered after the jump.
- Steps of deformation followed by inter-deformation isothermal heat treatments can promote recrystallisation. Static recrystallisation and static recovery occur during the inter-deformation steps. Shorter intervals for the isothermal treatments seem to have a more positive effect on recrystallisation than longer intervals.
- Due to the notably large grain size of the as-cast material, deformation occurs heterogeneously within a grain as well as nucleation during recrystallisation.
- Chemical segregation is small for the investigated as-cast microstructure, but it is difficult to be eliminated even for heat treatment at  $1150\text{ }^{\circ}\text{C}$  for 24 h. It suggests that temperatures close to the melting point are required to achieve complete chemical homogenisation.
- Multiple deformations and annealing steps are a suitable combination for effective grain refinement. Probably strains higher than 0.85 are required to achieve a homogenous microstructure.

## CRediT authorship contribution statement

**Ricardo Henrique Buzolin:** Conceptualization, Methodology, Formal analysis, Investigation, Writing – original draft, Writing – review & editing, Visualization. **Markus Masswohl:** Conceptualization, Methodology, Investigation, Writing – review & editing, Visualization. **Franz Miller Branco Ferraz:** Conceptualization, Methodology, Investigation, Writing – original draft, Writing – review & editing. **Konrad Chrzan:** Conceptualization, Methodology, Investigation, Writing – review & editing. **Tomasz Dudziak:** Conceptualization, Resources, Writing – review & editing. **Maria Cecilia Poletti:** Conceptualization, Resources, Writing – review & editing.

## Declaration of competing interest

The authors declare that they have no known competing financial interests or personal relationships that could have appeared to influence the work reported in this paper.

## Data availability

Data will be made available on request.

## Acknowledgements

The authors carried out this work under the following projects: KMM-VIN research fellowship from the European Virtual Institute on Knowledge-based Multifunctional Materials AISBL (KMM-VIN), and D-1303000107/CD-Laboratory for Design of High-Performance Alloys by Thermomechanical Processing with the support of the Christian Doppler Forschungsgesellschaft. Open access funding by the Graz University of Technology is also acknowledged.

## References

- [1] D.B. Miracle, O.N. Senkov, A critical review of high entropy alloys and related concepts, *Acta Mater.* 122 (2017) 448–511, <https://doi.org/10.1016/j.actamat.2016.08.081>.
- [2] E.P. George, D. Raabe, R.O. Ritchie, High-entropy alloys, *Nat. Rev. Mater.* 4 (8) (2019) 515–534, <https://doi.org/10.1038/s41578-019-0121-4>.
- [3] M.-H. Tsai, J.-W. Yeh, High-entropy alloys: a critical review, *Mater. Res. Lett.* 2 (3) (2014) 107–123, <https://doi.org/10.1080/21663831.2014.912690>.
- [4] Y.F. Ye, Q. Wang, J. Lu, C.T. Liu, Y. Yang, High-entropy alloy: challenges and prospects, *Mater. Today* 19 (6) (2016) 349–362, <https://doi.org/10.1016/j.mattod.2015.11.026>.
- [5] S. Huang, et al., Mechanism of magnetic transition in FeCrCoNi-based high entropy alloys, *Mater. Des.* 103 (2016) 71–74, <https://doi.org/10.1016/j.matdes.2016.04.053>.
- [6] B. Gludovatz, A. Hohenwarter, D. Catoor, E.H. Chang, E.P. George, R.O. Ritchie, A fracture-resistant high-entropy alloy for cryogenic applications (80–), *Science* 345 (6201) (2014) 1153–1158, <https://doi.org/10.1126/science.1254581>.
- [7] N. Kumar, et al., High strain-rate compressive deformation behavior of the Al<sub>0.1</sub>CrFeCoNi high entropy alloy, *Mater. Des.* 86 (2015) 598–602, <https://doi.org/10.1016/j.matdes.2015.07.161>.
- [8] P. Shi, et al., Enhanced strength–ductility synergy in ultrafine-grained eutectic high-entropy alloys by inheriting microstructural lamellae, *Nat. Commun.* 10 (1) (2019) 489, <https://doi.org/10.1038/s41467-019-08460-2>.
- [9] N. Kumar Katiyar, K. Biswas, J.-W. Yeh, S. Sharma, C. Sekhar Tiwary, A perspective on the catalysis using the high entropy alloys, *Nano Energy* 88 (2021), 106261, <https://doi.org/10.1016/j.nanoen.2021.106261>.
- [10] K. Li, W. Chen, Recent progress in high-entropy alloys for catalysts: synthesis, applications, and prospects, *Mater. Today Energy* 20 (2021), 100638, <https://doi.org/10.1016/j.mtener.2021.100638>.
- [11] M.S. Lucas, et al., Magnetic and vibrational properties of high-entropy alloys, *J. Appl. Phys.* 109 (7) (2011), 07E307, <https://doi.org/10.1063/1.3538936>.
- [12] V. Chaudhary, R. Chaudhary, R. Banerjee, R. V. Ramanujan, Accelerated and conventional development of magnetic high entropy alloys, *Mater. Today* 49 (2021) 231–252, <https://doi.org/10.1016/j.mattod.2021.03.018>.
- [13] P. Kumari, A.K. Gupta, R.K. Mishra, M.S. Ahmad, R.R. Shahi, A comprehensive review: recent progress on magnetic high entropy alloys and oxides, *J. Magn. Magn. Mater.* 554 (2022), 169142, <https://doi.org/10.1016/j.jmmm.2022.169142>.
- [14] H. Cheng, et al., Review—corrosion-resistant high-entropy alloy coatings: a review, *J. Electrochem. Soc.* 168 (11) (Nov. 2021), 111502, <https://doi.org/10.1149/1945-7111/ac34d0>.
- [15] X. Zhang, N. Zhang, B. Xing, S. Yin, An assessment of the high-temperature oxidation resistance of selected thermal sprayed high entropy alloy coatings, *J. Therm. Spray Technol.* 31 (4) (2022) 1386–1403, <https://doi.org/10.1007/s11666-022-01352-w>.
- [16] E.P. George, W.A. Curtin, C.C. Tasan, High entropy alloys: a focused review of mechanical properties and deformation mechanisms, *Acta Mater.* 188 (2020) 435–474, <https://doi.org/10.1016/j.actamat.2019.12.015>.
- [17] J. Chen, et al., A review on fundamental of high entropy alloys with promising high-temperature properties, *J. Alloys Compd.* 760 (15–30) (2018), <https://doi.org/10.1016/j.jallcom.2018.05.067>.
- [18] E. Ma, X. Wu, Tailoring heterogeneities in high-entropy alloys to promote strength–ductility synergy, *Nat. Commun.* 10 (1) (2019) 5623, <https://doi.org/10.1038/s41467-019-13311-1>.
- [19] H. Yu, et al., A brief review of metastable high-entropy alloys with transformation-induced plasticity, *Mater. Sci. Technol.* 36 (18) (2020) 1893–1902, <https://doi.org/10.1080/02670836.2020.1851437>.
- [20] L. Rogal, Y. Ikeda, M. Lai, F. Körmann, A. Kalinowska, B. Grabowski, Design of a dual-phase hcp-bcc high entropy alloy strengthened by  $\omega$  nanoprecipitates in the Sc-Ti-Zr-Hf-Re system, *Mater. Des.* 192 (2020), 108716, <https://doi.org/10.1016/j.matdes.2020.108716>.
- [21] M.C. Gao, B. Zhang, S.M. Guo, J.W. Qiao, J.A. Hawk, High-entropy alloys in hexagonal close-packed structure, *Metall. Mater. Trans. A* 47 (7) (2016) 3322–3332, <https://doi.org/10.1007/s11661-015-3091-1>.
- [22] X. Chang, M. Zeng, K. Liu, L. Fu, Phase engineering of high-entropy alloys, *Adv. Mater.* 32 (14) (2020), 1907226, <https://doi.org/10.1002/adma.201907226>.
- [23] Z. Savaedi, R. Motallebi, H. Mirzadeh, A review of hot deformation behavior and constitutive models to predict flow stress of high-entropy alloys, *J. Alloys Compd.* 903 (2022), 163964, <https://doi.org/10.1016/j.jallcom.2022.163964>.
- [24] R.R. Eleti, T. Bhattacharjee, L. Zhao, P.P. Bhattacharjee, N. Tsuji, Hot deformation behavior of CoCrFeMnNi FCC high entropy alloy, *Mater. Chem. Phys.* 210 (2018) 176–186, <https://doi.org/10.1016/j.matchemphys.2017.06.062>.
- [25] N. Prasad, N. Bibhanshu, N. Nayan, G.S. Avadhani, S. Suwas, Hot deformation behavior of the high-entropy alloy CoCuFeMnNi, *J. Mater. Res.* 34 (5) (2019) 744–755, <https://doi.org/10.1557/jmr.2018.500>.
- [26] M. Patnamsetty, A. Saastamoinen, M.C. Somani, P. Peura, Constitutive modelling of hot deformation behaviour of a CoCrFeMnNi high-entropy alloy, *Sci. Technol. Adv. Mater.* 21 (1) (2020) 43–55, <https://doi.org/10.1080/14686996.2020.1714476>.
- [27] C. Brown, T. McCarthy, K. Chadha, S. Rodrigues, C. Aranas, G.C. Saha, Constitutive modeling of the hot deformation behavior of CoCrFeMnNi high-entropy alloy, *Mater. Sci. Eng., A* 826 (2021), 141940, <https://doi.org/10.1016/j.msea.2021.141940>.
- [28] A.W. Abdelghany, et al., Hot deformation behavior and constitutive modeling of a cost-effective Al<sub>8</sub>Cr<sub>12</sub>Mn<sub>25</sub>Ni<sub>20</sub>Fe<sub>35</sub> high-entropy alloy, *J. Alloys Compd.* 928 (2022), 167028, <https://doi.org/10.1016/j.jallcom.2022.167028>.
- [29] H.T. Jeong, H.K. Park, K. Park, T.W. Na, W.J. Kim, High-temperature deformation mechanisms and processing maps of equiatomic CoCrFeMnNi high-entropy alloy, *Mater. Sci. Eng., A* 756 (2019) 528–537, <https://doi.org/10.1016/j.msea.2019.04.057>.
- [30] N. Haghdadi, S. Primig, M. Annasamy, P. Cizek, P.D. Hodgson, D.M. Fabijanic, On the hot-worked microstructure of a face-centered cubic Al<sub>0.3</sub>CoCrFeNi high entropy alloy, *Scripta Mater.* 178 (2020) 144–149, <https://doi.org/10.1016/j.scriptamat.2019.11.022>.
- [31] J. Wang, P. Yang, D. Wang, Constitutive equation and microstructure analysis of Al<sub>0.6</sub>CoCrFeNi high entropy alloy during hot deformation, *Philos. Mag. A* 102 (17) (2022) 1684–1707, <https://doi.org/10.1080/14786435.2022.2080292>.
- [32] W.J. Kim, H.T. Jeong, H.K. Park, K. Park, T.W. Na, E. Choi, The effect of Al to high-temperature deformation mechanisms and processing maps of Al<sub>0.5</sub>CoCrFeMnNi high entropy alloy, *J. Alloys Compd.* 802 (2019) 152–165, <https://doi.org/10.1016/j.jallcom.2019.06.099>.
- [33] N.D. Stepanov, et al., High temperature deformation behavior and dynamic recrystallization in CoCrFeNiMn high entropy alloy, *Mater. Sci. Eng., A* 636 (2015) 188–195, <https://doi.org/10.1016/j.msea.2015.03.097>.
- [34] J. Li, et al., High temperature deformation behavior of carbon-containing FeCoCrNiMn high entropy alloy, *J. Alloys Compd.* 747 (2018) 571–579, <https://doi.org/10.1016/j.jallcom.2018.02.332>.
- [35] A.J. Zaddach, C. Niu, C.C. Koch, D.L. Irving, Mechanical properties and stacking fault energies of NiFeCrCoMn high-entropy alloy, *J. Occup. Med.* 65 (12) (2013) 1780–1789, <https://doi.org/10.1007/s11837-013-0771-4>.
- [36] S. Qiu, et al., Influence of lattice distortion on stacking fault energies of CoCrFeNi and Al-CoCrFeNi high entropy alloys, *J. Alloys Compd.* 846 (2020), 156321, <https://doi.org/10.1016/j.jallcom.2020.156321>.
- [37] N.L. Okamoto, et al., Size effect, critical resolved shear stress, stacking fault energy, and solid solution strengthening in the CrMnFeCoNi high-entropy alloy, *Sci. Rep.* 6 (1) (2016), 35863, <https://doi.org/10.1038/srep35863>.
- [38] M.A. Hemphill, et al., Fatigue behavior of Al<sub>0.5</sub>CoCrCuFeNi high entropy alloys, *Acta Mater.* 60 (16) (2012) 5723–5734, <https://doi.org/10.1016/j.actamat.2012.06.046>.
- [39] N. Choi, K.R. Lim, Y.S. Na, U. Glatzel, J.H. Park, Characterization of non-metallic inclusions and their influence on the mechanical properties of a FCC single-phase high-entropy alloy, *J. Alloys Compd.* 763 (2018) 546–557, <https://doi.org/10.1016/j.jallcom.2018.05.339>.
- [40] G. Laplanche, P. Gadaud, O. Horst, F. Otto, G. Eggeler, E.P. George, Temperature dependencies of the elastic moduli and thermal expansion coefficient of an equiatomic, single-phase CoCrFeMnNi high-entropy alloy, *J. Alloys Compd.* 623 (2015) 348–353, <https://doi.org/10.1016/j.jallcom.2014.11.061>.

- [41] K. Huang, R.E. Logé, A review of dynamic recrystallization phenomena in metallic materials, *Mater. Des.* 111 (2016) 548–574, <https://doi.org/10.1016/j.matdes.2016.09.012>.
- [42] T. Sakai, A. Belyakov, R. Kaibyshev, H. Miura, J.J. Jonas, Dynamic and post-dynamic recrystallization under hot, cold and severe plastic deformation conditions, *Prog. Mater. Sci.* 60 (Mar. 2014) 130–207, <https://doi.org/10.1016/j.pmatsci.2013.09.002>.
- [43] N.K. Park, I.S. Kim, Y.S. Na, J.T. Yeom, Hot forging of a nickel-base superalloy, *J. Mater. Process. Technol.* 111 (1) (2001) 98–102, [https://doi.org/10.1016/S0924-0136\(01\)00489-7](https://doi.org/10.1016/S0924-0136(01)00489-7).
- [44] K.-Y. Tsai, M.-H. Tsai, J.-W. Yeh, Sluggish diffusion in Co–Cr–Fe–Mn–Ni high-entropy alloys, *Acta Mater.* 61 (13) (2013) 4887–4897, <https://doi.org/10.1016/j.actamat.2013.04.058>.
- [45] J. Dąbrowa, et al., Demystifying the sluggish diffusion effect in high entropy alloys, *J. Alloys Compd.* 783 (2019) 193–207, <https://doi.org/10.1016/j.jallcom.2018.12.300>.